

**Ultrafast coupling of coherent phonons with a nonequilibrium electron-hole plasma in GaAs**Amlan Kumar Basak,<sup>1</sup> Hrvoje Petek,<sup>1,\*</sup> Kunie Ishioka,<sup>2</sup> Evan M. Thatcher,<sup>3</sup> and Christopher J. Stanton<sup>3,†</sup><sup>1</sup>*Department of Physics and Astronomy, University of Pittsburgh, Pittsburgh, Pennsylvania 15260, USA*<sup>2</sup>*Nano Characterization Unit, National Institute for Materials Science, Tsukuba, 305-0047 Japan*<sup>3</sup>*Department of Physics, University of Florida, Gainesville, Florida 32611, USA*

(Received 3 December 2014; revised manuscript received 21 January 2015; published 2 March 2015)

We present a joint experimental theoretical study of the coupling of coherent phonons in bulk GaAs with a nonequilibrium electron-hole plasma following photoexcitation at the  $E_1$  gap by ultrafast laser pulses. In contrast to prior coherent phonon experiments where photoexcitation across the  $E_0$  gap generated electrons in the  $\Gamma$  valley, for the  $E_1$  gap excitation, the majority of the electrons are generated in the satellite  $L$  valleys. This leads to a drastically different situation from the previous studies because the damping of electrons is now faster due to the higher scattering rates in the  $L$  valley, and, in addition, the *diffusion* of carriers has a significant effect on the plasma response due to the shorter optical absorption depth of the pump-probe light. Reflectivity measurements show coherent phonon-plasmon oscillations, whose frequencies lie *between* the transverse and longitudinal optical phonon frequencies due to the heavy damping and change with time due to the diffusion of the plasma. We analyze the experimental data with a theoretical model that describes the time and density-dependent coupling of the coherent phonon and the electron-hole plasma as the photoexcited carriers diffuse into the sample on a subpicosecond time scale. The calculated phonon-plasmon dynamics qualitatively reproduce the experimentally observed time-dependent frequency.

DOI: [10.1103/PhysRevB.91.125201](https://doi.org/10.1103/PhysRevB.91.125201)

PACS number(s): 78.47.jg, 63.20.kd, 78.30.Fs

**I. INTRODUCTION**

A detailed understanding of the coherent many-body interactions between a photoexcited, nonequilibrium electron-hole (e-h) plasma and the lattice vibrations is important for understanding the electronic, optical, and transport properties of semiconductor materials and their devices at terahertz (THz) frequencies. Sudden, above band gap photoexcitation of a semiconductor with a femtosecond laser pulse creates quasiparticles in the valence and conduction bands under nonequilibrium conditions; the subsequent material response reveals the primary quasiparticle interactions as their energy, momentum, and spatial distributions evolve towards equilibrium [1–3]. Ultrafast optical techniques reveal distinct phases of the carrier-lattice dynamics, including time-dependent screening, carrier-carrier and carrier-lattice scattering, as well as carrier diffusion [4,5]. They have been employed for characterizing the electron and hole dynamics in pump-probe transmission and reflectivity, time-resolved photoluminescence, THz spectroscopy, four-wave mixing, and time-resolved two-photon photoemission experiments [4–11]. Femtosecond laser pulses have also been used to excite and observe the coherent  $q = 0$  optical phonon (coherent phonon) dynamics in a broad range of materials, including metals, semimetals, and semiconductors [3,8,12–18]. Impurity or photodoping of semiconductors introduces free carrier plasmas in the valence and conduction bands with frequencies typically in the THz range. In polar semiconductors, the coherent collective oscillation of the lattice ions can couple with that of the free charge carrier plasma of comparable frequency [19]; the coupling between them renormalizes their bare resonant frequencies and dephasing rates giving

rise to a new set of free-carrier density-dependent coupled modes on the time scale of screening [2]. In some cases, the carrier-lattice coupling can be sufficiently strong to even induce phase transitions on a femtosecond time scale [20,21]. Thus, monitoring the time evolution of the coherent THz oscillations through their associated longitudinal field following ultrafast laser excitation directly provides information on the quasiparticle dynamics and correlations as the photoexcited system evolves through various stages towards equilibrium.

Coherent phonons can be excited when photoexcitation of e-h pairs across the band gap of a semiconductor creates a displacive force on the lattice [22]. In the case of the (100) surface of impurity doped GaAs, the dominant coherent phonon excitation mechanism is transient depletion field screening (TDFS) where the photoexcited carrier plasma suddenly screens the electric field within the depletion layer at the crystal surface [23]. The trapping of carriers at the semiconductor-vacuum interface under equilibrium conditions creates a built-in field, which imposes a static stress on the ionic lattice. Upon photoexcitation, the built-in field accelerates free electrons and holes in the opposite directions whereby it is screened to suddenly release the stress. The step function force triggers the coherent longitudinal optical (LO) phonon oscillations where the Ga and As ions move in opposite directions so that the center of mass remains constant [3,13,24–26]. Simultaneously, screening of the bare lattice by the free carriers gives rise to the dressed modes of the coupled system.

The frequency of the pure (noninteracting) plasma oscillations  $\omega_{\text{pl}} = \sqrt{4\pi e^2 n / \epsilon_{\infty} m_{\text{pl}}}$  depends on the density  $n$  and mass  $m_{\text{pl}}$  of the free carriers, which comprise the plasma. The dephasing rate of the plasma  $\gamma_{\text{el}}$  also depends on  $m_{\text{pl}}$ : the carrier mass determines the density of states (DOS) of the free carrier bands and therefore the phase space for the carrier momentum scattering. The period and dephasing of the plasma

\*Corresponding author: petek@pitt.edu

†Corresponding author: stanton@phys.ufl.edu

oscillations define the time scale of screening of the Coulomb interaction, which forms the coupled modes of the interacting carrier-lattice system [2,5].

The coherent coupled mode dynamics for photoexcitation of carriers across the fundamental  $E_0$  gap of GaAs are already well understood from the pioneering papers of Dekorsy, Cho, Hase, and others [8,27–30]. At the fundamental gap, the electrons and holes are photoexcited near the conduction band minimum and valence band maximum both at the  $\Gamma$  point, where they remain until they recombine across the gap on a time scale that is much longer than the phonon dephasing time. The spatial distributions of electrons and holes are quasistationary after the initial acceleration; their diffusion on the time scale of LO phonon dephasing can be ignored due to the large optical penetration depth compared with the depletion layer thickness. Consequently, simple modeling of the coherent phonon dynamics with quasistationary LO-electron and LO-hole coupling is a good approximation. The electron plasmon frequencies in the  $\Gamma$  valley are large due to a low value of  $m_{pl}$ . In multivalley semiconductors such as GaAs, however, the photoexcitation can populate different bands and valleys with a heavier  $m_{pl}$  within the valence and conduction bands, depending on the excitation wavelength [3,31]. The larger value of  $m_{pl}$  results in a lower  $\omega_{pl}$  and higher  $\gamma_{el}$ .

Following photoexcitation, the plasma dynamics evolve due to the redistribution of free carriers among the different valleys in the conduction band and scattering between the different valence bands [3,11,32] as well as by their spatial diffusion [33] on time scales that are comparable to the LO phonon period of 115 fs. Consequently, couplings of the lattice with photoexcited multicomponent plasma can be far more complicated when excited at the  $E_1$  gap of GaAs, which creates electron-hole pairs predominantly in the  $L$  valley and with large excess energy in the  $\Gamma$  valley (Fig. 1); there the carrier redistribution among the  $\Gamma$ ,  $L$ , and  $X$  valleys occurs on a tens of femtoseconds time scale [11]. Thus, studying the density- and time-dependent behavior of the coupled plasmon-phonon modes upon  $E_1$  gap excitation can reveal details of the nonequilibrium carrier-lattice dynamics in the near-surface region for different initial plasma densities and carrier distributions.

Here, we investigate the carrier density dependence of the plasmon and phonon properties after ultrafast optical excitation with  $\sim 10$  fs pulses at 400 nm (3.11 eV), whose spectra span the  $E_1$  and  $E_1 + \Delta_1$  critical points of GaAs at 3.01 and 3.25 eV [34]. Figure 1 shows the band structure of GaAs and the optical transitions that can be excited at this wavelength from a 30 band  $\mathbf{k} \cdot \mathbf{p}$  calculation [35,36]. We perform time domain measurements of transient reflectivity of GaAs in the electro-optic (EO) sampling mode to record the time-dependent longitudinal polarization field. We find that the frequency of the plasmon-phonon mode changes rapidly on the time scale of LO phonon period due to the intervalley redistribution and density decrease of the photoexcited carriers from the probed region. The experimentally observed time-dependent frequency is qualitatively reproduced by our theoretical model, including photoexcitation into  $\Gamma$  and  $L$  valleys and the diffusion of carriers away from the surface and into the bulk.

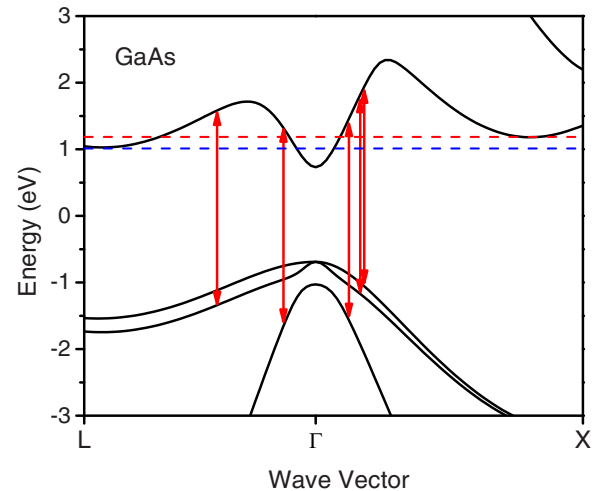


FIG. 1. (Color online) Allowed energy transitions in GaAs for pumping by a 400 nm (3.11 eV) pump pulse. The electronic structure is calculated from a 30 band  $\mathbf{k} \cdot \mathbf{p}$  calculation. Holes are created in all three valence bands. Electrons are generated directly in both the  $\Gamma$  and the  $L$  valleys. All conduction band electrons are energetically able to scatter among the  $\Gamma$  and the satellite  $X$  and  $L$  valleys. The dotted blue and red lines mark the bottoms of the  $L$  and  $X$  valleys, respectively.

This paper is organized as follows. Section II describes the experimental setup for transient reflectivity measurements; Sec. III presents the experimental results; Sec. IV presents a model for the time-dependent coupled plasmon-phonon modes due to a spatially nonuniform carrier density and subpicosecond time scale transport; and Sec. V gives the discussion and conclusions.

## II. EXPERIMENTAL SETUP

The sample studied is a (100) oriented  $n$ -type GaAs doped with Si at  $n_d = 2 \times 10^{18} \text{ cm}^{-3}$ . The depletion layer thickness is estimated to be  $\sim 22$  nm, and the built-in field 400 kV/cm points from the sample to the surface [37]. Pump-probe reflectivity measurements are performed under ambient conditions using the second harmonic of a Ti:sapphire laser with 70 MHz repetition rate (3.11 eV photon energy and 10 fs duration). Details of the experimental technique have been described previously [3,16,18,31]. The pump and probe beams, linearly polarized along the [011] and [001] crystallographic axes, are focused using a concave mirror with either 50, 100, or 150 mm focal length onto the same spot on the sample surface with a typical beam diameter of  $d = 10 - 40 \mu\text{m}$ . The beams are incident onto the sample with angles of  $\sim 5^\circ$  and  $\sim 15^\circ$  from the surface normal. The density of the photoexcited plasma of  $n_{exc} \sim 10^{18} - 10^{20} \text{ cm}^{-3}$  is approximately estimated by  $(1 - R)Q\alpha/\pi d^2$ , where  $R$  is the reflectivity of the sample (0.477 at 400 nm),  $Q$  the number of incident photons, and  $1/\alpha = 15$  nm the optical penetration depth [38]. The effective probe depth is given by  $1/(2\alpha) = 7.5$  nm because the probe light transverses the medium twice. The pump-induced change in the anisotropic reflectivity ( $\Delta R_{eo} = \Delta R_H - \Delta R_V$ ) is measured in the EO configuration by detecting the difference between the vertically (V) and horizontally (H) polarized

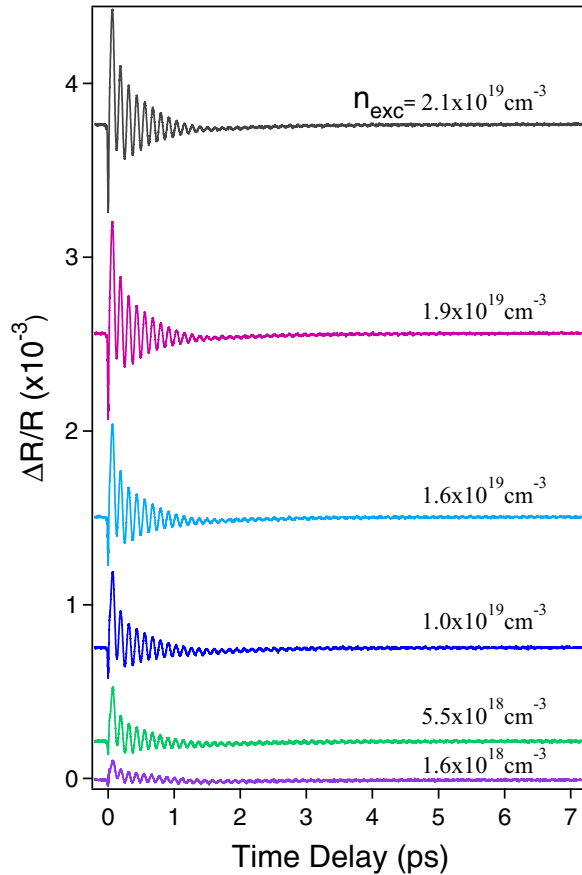


FIG. 2. (Color online) Anisotropic reflectivity as a function of time delay for different photoexcitation levels. Individual scans are offset in the vertical direction for clarity.

components of the reflected probe light along the  $[011]$  and  $[0\bar{1}1]$  crystallographic axes. The EO detection scheme enables subtraction of the intense isotropic change in the complex index of refraction, thereby enabling sensitive detection of the longitudinal polarization [13]. The transient reflectivity signal is averaged with a digital oscilloscope for 5000–20 000 scans using a fast-scan (10–20 Hz) pump-probe delay modulation [3,16].

### III. RESULTS

Figure 2 shows the anisotropic reflectivity change of the GaAs surface as a function of time delay for different photoexcited carrier densities  $n_{\text{exc}}$  [39]. The coherent response consists of three main components: (i) a nearly instantaneous and strongly damped transient electronic response; (ii) a fast ( $<1$  ps) decaying oscillatory response; and (iii) a long-lived ( $\sim 4$  ps) oscillatory response. The Fourier transform (FT) spectra of the oscillatory signals (Fig. 3) show, correspondingly, a broad electronic background on top of which at low  $n_{\text{exc}}$  there is a sharp peak at 8.7 THz; with increasing laser fluence this peak turns into a high frequency shoulder of another broad band. This new band shifts to a lower frequency and grows in intensity with increasing laser fluence. The frequency of 8.7 THz corresponds to the bare LO phonon reported in previous papers [31,40]. The broad band shifts from approximately the

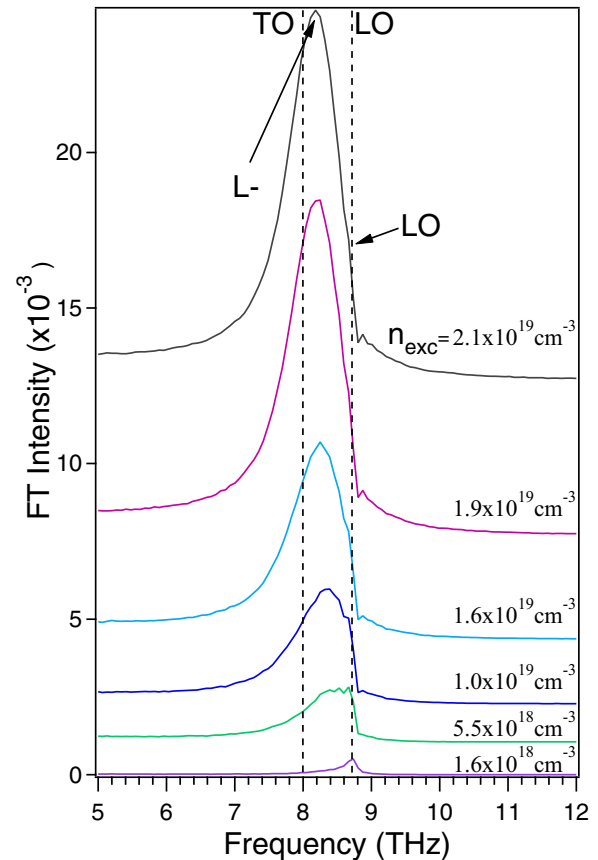


FIG. 3. (Color online) FT power spectra of the time-dependent reflectivity signals showing bare LO phonon response and lower branch of the plasmon-phonon coupled mode ( $L_-$ ). The dotted lines indicate the bare TO and LO phonon frequencies. Individual spectra are displaced in vertical direction.

LO to the transverse optical (TO) phonon ( $\omega_{\text{TO}} = 8.0$  THz) frequency limits. As we will show formally in Sec. IV, the carrier density-dependent frequency identifies this mode as the lower branch of the LO phonon-plasmon coupled modes ( $L_-$ ) with predominantly phononic character. The upper branch ( $L_+$ ) with predominantly plasmonic character will be briefly discussed in Sec. IV [41]. The appearance of the  $L_-$  mode in the reststrahlen gap between the LO and TO frequencies is expected for a strongly damped plasma, as has been observed in the previous Raman studies on the  $p$ -type GaAs [42–44]. We will discuss the frequency and damping behavior of the  $L_-$  mode in detail in the following section.

From the FT power spectra we extract the intensities of the bare LO phonon and  $L_-$  modes and study their behavior with changing photoexcited carrier density. The  $L_-$  mode has an asymmetric lineshape, and its width varies with the excitation density; therefore, its intensity is obtained by digital integration of the peak area. Where the LO mode has a significant contribution, its weight is subtracted from the total coherent response based on its frequency and dephasing times assuming a Lorentzian lineshape. The extracted peak intensity vs the peak carrier density for two excitation regimes corresponding to  $n_{\text{exc}}$  of  $1.6 \times 10^{18} - 2.1 \times 10^{19} \text{ cm}^{-3}$  is reported in Fig. 4(a) and  $3.1 \times 10^{19} - 2.7 \times 10^{20} \text{ cm}^{-3}$  in Fig. 4(b). In the lower

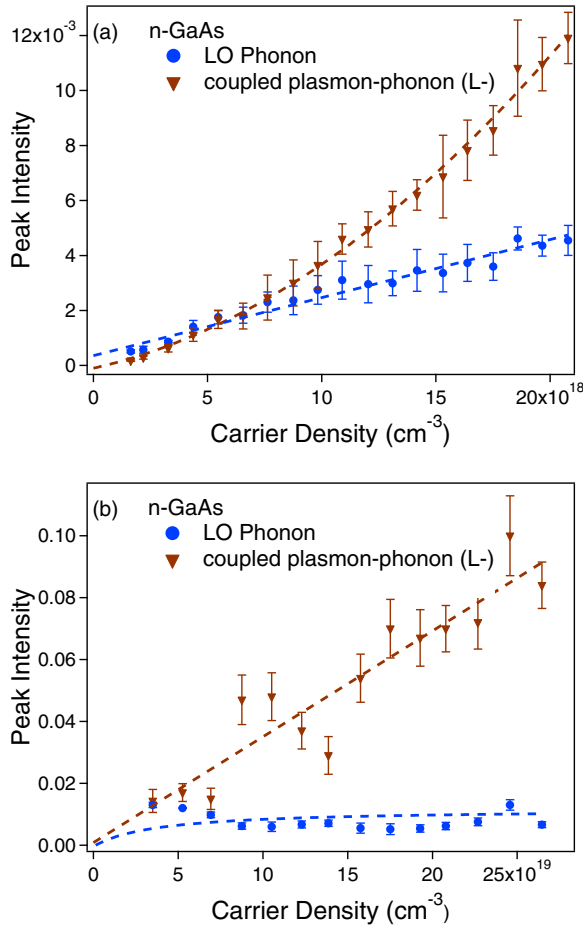


FIG. 4. (Color online) Intensities of the LO phonon and  $L_-$  contribution to the FT spectra with changing carrier densities for two carrier density regimes.

density regime [Fig. 4(a)], the LO phonon intensity increases nearly linearly with increasing carrier density, indicating a sublinear increase of the intensity. The intensity, frequency, and decay time of the coherent response are independent of the pump pulse polarization in the investigated  $<10^{19} \text{ cm}^{-3}$  density range [45], indicating that its excitation mechanism is the TDFS, as is the case for the 800 nm excitation [31]. This is an indication that the anisotropic contributions to the generation and relaxation dynamics, such as the deformation potential interaction, are considerably smaller for GaAs, unlike what we found previously for Si [46].

Above the critical density of  $\sim 3 \times 10^{19} \text{ cm}^{-3}$ , further increasing the laser fluence does not increase the driving force for excitation of the bare coherent LO phonons [Fig. 4(b)]. Similar saturation was observed in the emission of coherent acoustic phonons in GaAs by inverse piezoelectric effect [47]. The saturation is consistent with the complete screening of the depletion field; additional carriers above the critical density for releasing the lattice strain do not contribute to the driving force for the TDFS mechanism. This behavior is quite similar to what was observed for  $n$ -doped GaAs with pumping and probing near the fundamental band gap [40], although the critical density with 400 nm excitation is somewhat higher than that of a similarly doped sample. The higher critical density may

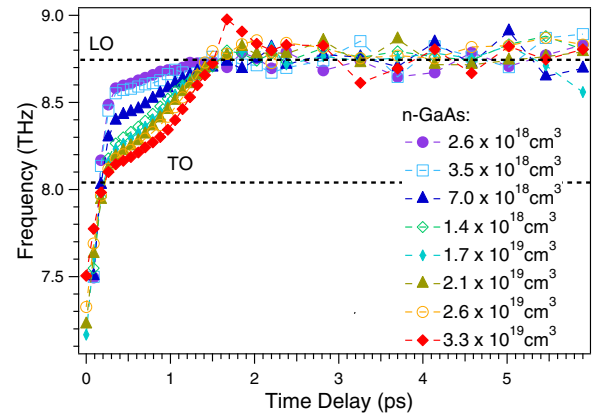


FIG. 5. (Color online) The time-dependent frequency change of the coherent oscillations from a time-windowed FT analysis.

reflect the higher effective carrier mass with 400 nm excitation, which reduces  $\omega_{\text{pl}}$  for comparable carrier density. In the higher density regime, the  $L_-$  intensity continues to increase linearly with the pump power because the amplitude of the charge-density fluctuations grows with the plasma density.

The coupled mode frequency depends on the pump density but also evolves with time delay as the photoexcited carrier density decreases. This can be visualized by performing time-windowed FT analysis of the coherent reflectivity responses. Here we use a Gaussian time window with full width at half-maximum (FWHM) of 293 fs, whose center position is scanned along the time delay axis. The frequency of the time-windowed FT peak is plotted in Fig. 5 as a function of the position of the time window for different pump densities. For the time-window position of  $<300$  fs, which is comparable with the time-window width and the dynamics reflecting the sudden turning of the force, the frequency upshifts steeply toward the TO frequency. Between 0.3 and 1.5 ps, the frequency upshifts from the TO toward the LO frequency limits. After 1.5 ps, the frequency stays at the LO frequency. The frequency at 0.3 ps is lower, i.e., closer to the TO frequency limit, for higher pump density. The time evolution in the first 1.5 ps can be interpreted in terms of the creation and decay of the  $L_-$  mode through the sudden creation of photocarriers, their diffusion from the surface, and the damping of the plasmon mode, as will be discussed in Sec. III.

We also extract decay times of the coherent modes. The decay times of the fast decaying  $L_-$  mode as a function of the carrier density are obtained by fitting the fast decaying oscillatory signal to an exponentially damped harmonic oscillator model. The decay times, which are reproduced in Fig. 6, show different trends in the low and high carrier density regimes; at lower densities (between  $1.6 \times 10^{18} \text{ cm}^{-3}$  to  $2.1 \times 10^{19} \text{ cm}^{-3}$ ), the decay times decrease from 0.93 to 0.48 ps, but at higher densities they saturate at around 0.45 ps.

The decay of the  $L_-$  mode, because it is a mixture, has contributions from both the plasmon and the bare LO phonon decay [8], but it is dominated by the stronger plasmon damping. In Raman scattering measurements, it was observed that the decay rate of the coupled plasmon-phonon mode increases linearly with the doped electron density [48]. This is consistent with theoretical calculations [49]. The coupled mode decay

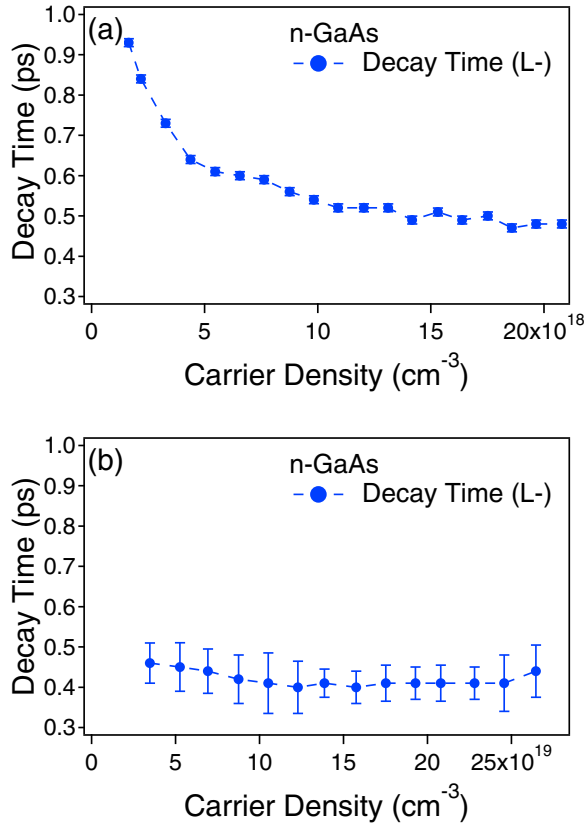


FIG. 6. (Color online) Coupled mode ( $L_-$ ) decay times with increasing carrier density for two carrier density regimes.

upon the  $E_1$  gap excitation is comparable at low densities, but at high densities it becomes considerably faster than found in n-GaAs when excited at the fundamental  $E_0$  gap where the doped carriers dominate the dynamics [40,50]. The damping is nevertheless slower than that for p-doped GaAs at 800 nm [50]. The observed carrier density dependent  $L_-$  mode dephasing can be understood, therefore, as being dominated by the slow damping of the doped  $\Gamma$  valley electrons for low fluence excitation, which is overtaken by the faster dephasing of the photodoped carriers at the high fluence. This is because the heavy carriers created with  $E_1$  gap excitation, i.e., the valance band holes and  $L$  valley electrons, undergo faster momentum scattering, as already discussed.

The decay times for the bare LO phonon mode are extracted by fitting another exponentially damped harmonic oscillator to the EO signal for time delays  $\tau > 2$  ps after the  $L_-$  mode has decayed. The decay time of this mode is not dependent on the instantaneous photocarrier density (Fig. 7). The measured decay time of  $\sim 3$  ps for the bare LO phonon is in the range of reported values in several experimental studies for different GaAs samples at room temperature [8,48]. The bare LO phonon signal can have contributions from both the residual coherent response after the plasma response has dephased, or it may come from the low-density wings of the transverse Gaussian carrier distribution [51]. The decay of the LO phonon in GaAs most likely is determined by anharmonic coupling with the acoustic phonons, with a zone center LO mode decaying into two zone edge acoustic phonons [48,52,53].

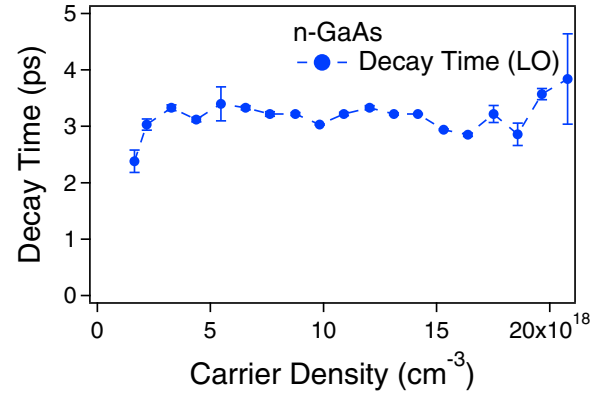


FIG. 7. (Color online) LO phonon decay time with increasing carrier density.

This process can simultaneously conserve both momentum (wavevector) and energy and typically has a decay time ranging from 4 to 8 ps, depending on the sample temperature.

Next we consider theoretically the dynamical responses of GaAs, which give rise to the observed photocarrier density and delay time-dependent behavior of the coupled plasmon-phonon modes.

## IV. THEORY AND MODELING

### A. Coupled plasmon-phonon modes

Modeling the transient oscillations representing the interaction of the photoexcited nonequilibrium e-h plasma with the GaAs lattice on the femtosecond time scale is a formidable task. The response has contributions both from the phonons as well as the plasmons, which interact with each other through the Coulomb interaction leading to the coupled plasmon-phonon modes. Moreover, the plasma has contributions from holes in multiple valence bands and electrons distributed anisotropically among multiple conduction band valleys ( $\Gamma$ ,  $L$ ,  $X$ ). The transient response is obtained by solving the equations for the *coupled plasmon-phonon modes*:

$$\begin{aligned} \frac{\partial^2 \mathbf{P}}{\partial t^2} + \gamma_{\text{el}} \frac{\partial \mathbf{P}}{\partial t} + \omega_{\text{pl}}^2 \mathbf{P} &= \frac{e^2 N(t)}{\epsilon_{\infty} m_{\text{pl}}} (\mathbf{E} - 4\pi \gamma_{12} \mathbf{W}) \\ \frac{\partial^2 \mathbf{W}}{\partial t^2} + \gamma_{\text{ph}} \frac{\partial \mathbf{W}}{\partial t} + \omega_{\text{LO}}^2 \mathbf{W} &= (\gamma_{12} / \epsilon_{\infty}) (\mathbf{E} - 4\pi \mathbf{P}). \end{aligned} \quad (1)$$

Here  $\mathbf{P}$  is the electronic polarization,  $\mathbf{W}$  is the normalized lattice displacement ( $\mathbf{W} = \sqrt{\rho} u$  where  $u$  is the optical mode displacement and  $\rho$  the density), and  $m_{\text{pl}}$  is the plasmon (optical) mass of the carrier. The plasmon and phonon mode damping constants are  $\gamma_{\text{el}}$ ,  $\gamma_{\text{ph}}$ , and we note that in the absence of coupling, their decay rates are given by  $\frac{\gamma_{\text{el}}}{2}$ ,  $\frac{\gamma_{\text{ph}}}{2}$ , respectively.  $\omega_{\text{LO}}$  and  $\omega_{\text{pl}}$  are the already defined LO phonon and the plasmon frequencies. The coupling between the plasmons and the phonons is given by  $\gamma_{12} = \omega_{\text{TO}} \sqrt{(\epsilon_0 - \epsilon_{\infty}) / 4\pi}$ , where  $\epsilon_0$  and  $\epsilon_{\infty}$  are the low and high frequency dielectric constants. The term  $N(t)$  represents the generation of photoexcited carriers by the pump laser pulse.  $\mathbf{E}$  is a static applied electric field, which can be internal, e.g., the surface depletion field, or external.

Photoexcitation of GaAs by a 400 nm 10 fs laser pulse creates carriers in all three conduction band valleys, the  $\Gamma$ ,  $X$ ,

and  $L$  and three valence bands, the heavy hole, the light hole, and the spin-orbit split hole band. This is illustrated in Fig. 1, where we show the electronic band structure of GaAs.

As previously noted, the excitation is dominated by the  $E_1$  and  $E_1 + \Delta_1$  critical points, corresponding to transitions from the heavy hole and light hole valance bands directly into the  $L$  valley of the conduction band. While there are optical transitions directly into both the  $\Gamma$  and the  $L$  valley, the dynamics are dominated by the  $L$  valley carriers. Although the  $\Gamma$  valley excitation has larger transition moments, the  $L$  valley has a higher joint DOS. Therefore, according to the  $\mathbf{k} \cdot \mathbf{p}$  calculation of the electronic bands, the initial  $L$  valley population that is created by photoabsorption is five times larger than that of the  $\Gamma$  valley. Moreover, the  $\Gamma$  valley electrons rapidly scatter within  $<20$  fs via intervalley deformation potential phonon scattering into both of the satellite  $X$  and  $L$  valleys [11]. There is no direct photoexcitation into the conduction band  $X$  valley; rather electrons scatter from either the  $\Gamma$  or  $L$  valleys. Light to heavy hole valence band scattering also occurs on a hundred fs time scale similar to Ge [54,55].

As a result of the multiband and multivalley excitation and rapid carrier scattering, the electronic system can be considered as a coupled six component plasma consisting of  $\Gamma$ ,  $X$ , and  $L$  electrons and heavy, light, and split off holes. A full description of the coupled carrier-phonon system should include, in addition to Eq. (1), five additional equations for each of the carrier types as well as the coupling and scattering terms between and within each type to take into account of the ultrafast generation, interaction, and decay of all carriers. Accounting of each type of carrier interacting with the lattice is not justified, however, because experiments show evidence for only a *single effective* plasma response with a frequency and damping that subsumes the complexity of the multicomponent plasma.

To proceed, we simplify the coupled mode equations in Eq. (1) by setting the electric field to zero. We can then assume the forms

$$\begin{aligned} \mathbf{P} &= \mathbf{P}_0 e^{-i\omega t} \\ \mathbf{W} &= \mathbf{W}_0 e^{-i\omega t}, \end{aligned} \quad (2)$$

which allow us to determine the eigenmodes of the coupled set of differential equations. We find that the eigenmodes of the equation are given by solutions to

$$\begin{aligned} \omega^4 + \omega^3(i\gamma_{\text{ph}} + i\gamma_{\text{el}}) - \omega^2(\omega_{\text{LO}}^2 + \gamma_{\text{el}}\gamma_{\text{ph}} + \omega_{\text{p}}^2) \\ - \omega(i\omega_{\text{LO}}^2\gamma_{\text{el}} + i\omega_{\text{pl}}^2\gamma_{\text{ph}}) \\ + \omega_{\text{pl}}^2\{\omega_{\text{LO}}^2 - 4\pi(\gamma_{12}^2/\epsilon_{\infty})\} = 0. \end{aligned} \quad (3)$$

Eq. (3) can be solved to find the frequencies of the coupled modes,  $L_-$  and  $L_+$ . We note the solution to Eq. (3) is formally equivalent to solving for the zeroes of the dielectric function

$$\epsilon(\omega) = \epsilon_{\infty} \left[ 1 - \frac{\omega_{\text{pl}}^2}{\omega^2 + i\gamma_{\text{el}}\omega} + \frac{\omega_{\text{LO}}^2 - \omega_{\text{TO}}^2}{\omega_{\text{TO}}^2 - i\gamma_{\text{ph}}\omega - \omega^2} \right]. \quad (4)$$

Eq. (4), however, is usually used in the continuous wave (cw) excitation limit (for Raman spectroscopy, for instance) where the carriers come from doping, and, as a result, *only one type of carrier* is present. In addition, Eq. (4) cannot treat the initial, transient response to the photoexcitation used in pump-probe spectroscopy, whereas Eq. (1) can. The solutions

TABLE I. The optical masses used in the calculations of plasma frequencies for different carrier types in GaAs.  $m_0$  is the free electron mass.

Valley	Mass
$\Gamma$	$0.063 m_0$
$L$	$0.11 m_0$
$X$	$0.27 m_0$
Light hole	$0.08 m_0$
Heavy hole	$0.5 m_0$
Split-off hole	$0.15 m_0$
$L$ and heavy hole ( $m^*$ )	$0.09 m_0$

to Eq. (3) [or Eq. (4)] are still useful and provide valuable insight.

From Eq. (3), we see that by making the substitution  $z = i\omega$ , we get a fourth-order equation in the complex variable  $z$  with *real* coefficients. This means that the roots of the  $z$  equation are either real or there is an even number of complex roots that occur in conjugate pairs. For the complex variable  $\omega$ , this means that the roots occur in pairs,  $\omega = \pm\omega_r - i\omega_i$  or that they are completely imaginary (such as in the case of the overdamped plasmon mode near zero carrier density). This of course makes physical sense because if there is a positive real frequency solution, there should also be a negative real frequency solution, and both should have the same damping.

The solutions to Eq. (3) depend on carrier density and type (mass) through the plasma frequency. Referring to the band structure of GaAs in Fig. 1, for the  $\Gamma$  valley where the conduction band is locally spherical, the carrier mass  $m_{\text{pl}}$  is just the effective mass for that valley (i.e., the  $\Gamma$  valley electrons). For the  $X$  and  $L$  valleys where the conduction band is locally ellipsoidal,  $m_{\text{pl}}$  is a weighted average of the longitudinal and transverse masses given by  $1/m_{\text{pl}} = 1/(3m_l) + 2/(3m_t)$ , which is often called the *optical mass* [56]. Because the smaller transverse mass is weighted by a factor of two compared to the longitudinal mass, screening by carriers in the  $X$  and  $L$  valleys is not as ineffective as one might infer from the curvatures of the conduction band potential in Fig. 1. In fact, from masses listed in Table I, we see that the optical mass for the  $L$  valley is only  $0.11 m_0$ , which is less than a factor of two larger than for the  $\Gamma$  valley.

Some insight in the plasma response is gained if one looks at the bare (noninteracting) plasma frequencies as a function of density for different bands/valleys (and hence different effective masses) without the inclusion of any damping or coupling and assuming that the bands and valleys can be approximated with parabolic dispersions over the density range. The calculated plasma frequencies for the six types of carriers as a function of their density are shown in Fig. 8. The parameters we use for the effective (optical) masses are shown in Table I.

The curves in Fig. 8 tell us the densities at which a given type of carrier interacts strongly with the phonons leading to the renormalized  $L_-$  and  $L_+$  modes. When the plasma frequency is close to the LO or TO frequency, then the eigenmodes are strongly coupled and they mix. This gives rise to the  $L_-$  and  $L_+$  coupled modes. If the carrier density and hence plasma

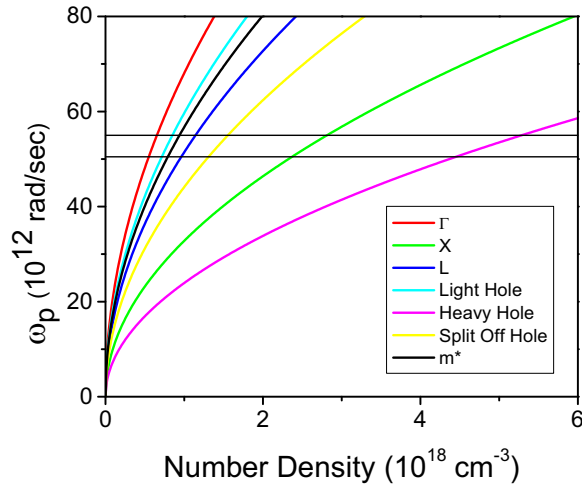


FIG. 8. (Color online) The noninteracting plasma frequency  $\omega_{pl} = \sqrt{4\pi n e^2 / (\epsilon_\infty m_{pl})}$  for various excitation densities using the respective masses for the three conduction valleys ( $\Gamma$ ,  $X$ ,  $L$ ) and three valance bands (heavy hole, light hole, and spin-orbit split holes). When the curves cross the solid lines representing the LO and TO frequencies, they interact strongly with the phonons. The black line ( $m^*$ ) corresponds to including both the  $L$  valley electrons and the heavy holes in the plasma frequency, that is,  $\omega_{pl} = \sqrt{(4\pi n e^2 / \epsilon_\infty)(1/m_L + 1/m_{HH})}$ .

frequency is small, then the coupled modes are only weakly coupled and are given approximately by a plasmlike and a LO phononlike modes. For example, heavy holes (purple line) at the top of the valance band need to reach a density of about  $4 - 5 \times 10^{18} \text{ cm}^{-3}$  to interact, whereas  $\Gamma$  valley electrons (red line) at the bottom of the conduction band can strongly interact at carrier densities less than  $1 \times 10^{18} \text{ cm}^{-3}$ . In the photoexcitation experiment with 400 nm light, most electrons and holes will be excited to or scatter into the  $L$  valley of the conduction band and the heavy hole subband of the valance band in less than the period of LO phonon vibration. Both will contribute to the plasma response with the frequency of the plasmon given by the effective mass,  $m^*$ , where  $1/m^* = 1/m_L + 1/m_{HH}$ , which yields  $m^* = 0.09 m_0$ . The frequency of the combined heavy hole and  $L$  valley plasmon as a function of the carrier density is shown by the black line in Fig. 8. As we can see in Fig. 8, the effective plasma frequency as a function of density is most similar to that of the light hole plasma, but it is not too different from the plasma frequency of the  $\Gamma$  valley electrons.

The exact numerical solutions of Eq. (3) including the effects of both mixing and damping for the coupled modes are shown in Fig. 9 using the above defined  $m^*$  for the plasmon mass, which includes the heavy hole and the  $L$  valley carriers together. Figure 9 shows the real (a) and imaginary (b) parts of both the  $L_+$  and  $L_-$  modes. We note that for weaker damping (40 THz), the “plasmonlike” mode is similar to that shown in Fig. 8 but shows level repulsion (hybridization) when the plasmon mode crosses the LO and TO phonon energies.

When coherent phonons are generated with 800 nm excitation near the fundamental band gap of GaAs [8,29], the damping is lower because the momentum scattering rate for the electrons in the  $\Gamma$  valley is slower than for excitation at

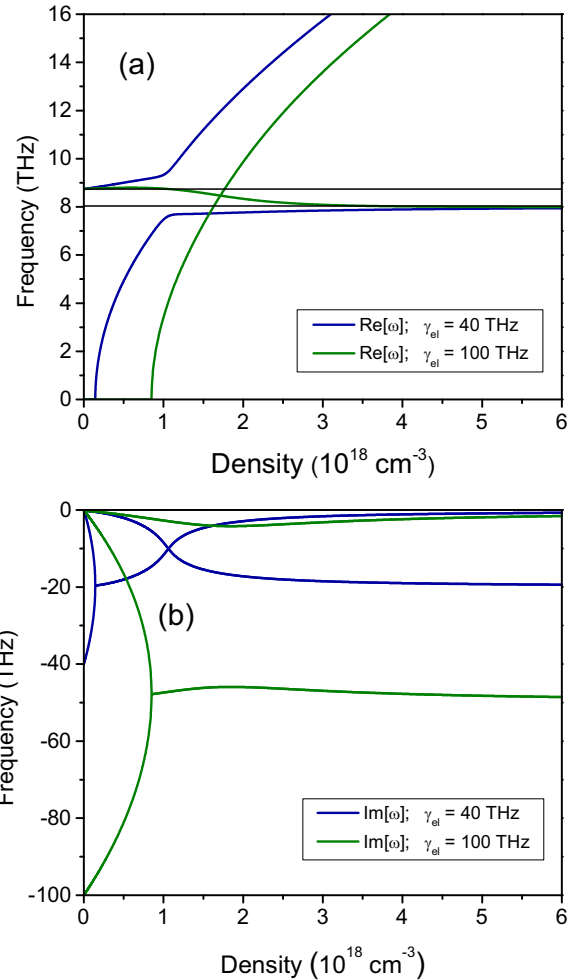


FIG. 9. (Color online) The real (a) and imaginary (b) parts of the coupled plasmon-phonon roots for weaker (40 THz) and stronger (100 THz) damping. The  $m^*$  mass includes the effects of the  $L$  valley electrons and the heavy holes. (a) For weak damping (40 THz), there are no solutions to the coupled equations where the real part lies between  $\omega_{TO}$  and  $\omega_{LO}$ . For strong damping, the real part of the solution can exist between  $\omega_{TO}$  and  $\omega_{LO}$ ; there is no plasmlike solution for densities  $< 10^{18} \text{ cm}^{-3}$ . (b) The imaginary parts of the roots cross for weaker damping (40 THz) but do not cross for stronger damping. The phonon damping rate in both cases is  $\gamma_{ph} = 0.2 \text{ THz}$ . Note that in this and subsequent figures, we divide the real part of the frequency by  $2\pi$ , but do not divide the imaginary part by  $2\pi$ .

400 nm, where it is much faster due to the increased DOS in the  $L$  and  $X$  valleys. In the low damping case, there is no solution for Eq. (3), where the real part of the frequency lies between the bare  $\omega_{TO}$  and  $\omega_{LO}$  frequencies. In contrast, for higher damping (100 THz), as shown in Fig. 9(a), the real part of the roots can lie between the  $\omega_{TO}$  and  $\omega_{LO}$  frequencies. The higher damping will also cause the necessary density for the crossing of the two roots to increase. For instance, in Fig. 8 for the  $m^*$  plasmon mode, we see that the noninteracting plasmon lies between the  $\omega_{TO}$  and  $\omega_{LO}$  frequencies at a carrier density of about  $1 \times 10^{18} \text{ cm}^{-3}$ , but for the strong damping (100 THz) case in Fig. 9(a), it is closer to  $2 \times 10^{18} \text{ cm}^{-3}$ . The existence of roots between the TO and LO frequencies in the strongly damped case has been observed experimentally in previous Raman

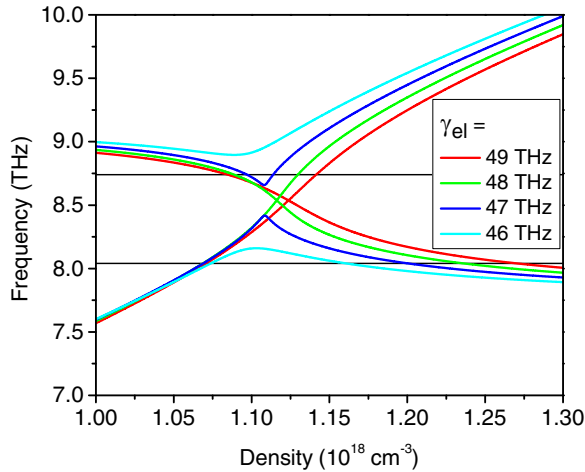


FIG. 10. (Color online) The real part of the coupled mode frequency for the critical values of the plasmon damping constant between 46 and 49 THz. For 48 THz and higher, the real roots cross between  $\omega_{\text{TO}}$  and  $\omega_{\text{LO}}$ .

scattering measurements on *p*-doped GaAs [42–44], as well as time-resolved second harmonic generation measurements of coherent phonons at the surface of GaAs [30].

Figure 9(b) shows the imaginary parts of the roots for  $\gamma_{\text{el}} = 40$  and 100 THz. The phonon damping is given by  $\gamma_{\text{ph}} = 0.2$  THz. For low damping (40 THz), we see that the imaginary parts of the roots cross; as the modes change their dominant character, their effective damping rates also switch through the crossing region [41]. For high damping (100 THz), however, there is no crossing. Rather at the lowest carrier densities, we see that the plasmonlike mode is overdamped (and the imaginary part of the root bifurcates). This leads to the finite value of density when the plasmonlike mode becomes nonzero in Fig. 9(a). We also see that the damping of the “phononlike” mode is larger than  $\gamma_{\text{ph}}$ . This comes from the mixing of the modes, with higher damping of the plasmon  $\gamma_{\text{el}}$  leading to a larger damping.

The condition for the real part of the roots to start appearing in the reststrahlen gap between  $\omega_{\text{TO}}$  and  $\omega_{\text{LO}}$  occurs when  $\gamma_{\text{el}}$  is slightly less than  $2\pi\omega_{\text{TO}}$  (for the plasmon mass  $m^*$  and a phonon damping constant of 0.2 THz). Behavior of the real part of the frequency of the coupled modes near this critical value is shown in Fig. 10. Even for  $\gamma_{\text{el}} = 46$  THz, the roots lie in the gap, but it is not until  $\gamma_{\text{el}} = 48$  THz that they actually cross.

In Fig. 11, we show the phononlike roots as a function of carrier density for types of carriers (as shown in Table I). In (a) we plot the roots as a function of density for  $\gamma_{\text{el}} = 100$  THz and in (b) for  $\gamma_{\text{el}} = 200$  THz. It can be concluded that having the real phononlike root to vary between the  $\omega_{\text{LO}}$  and  $\omega_{\text{TO}}$  limits over a wide carrier density range, such as observed in the experiments, requires a large ( $>100$ –200 THz) plasmon damping.

### B. Carrier dynamics and diffusion

The results presented so far suggest high ( $>100$  THz) damping rates for the plasma oscillations in the coherent phonon measurements with 400 nm light. In other coherent

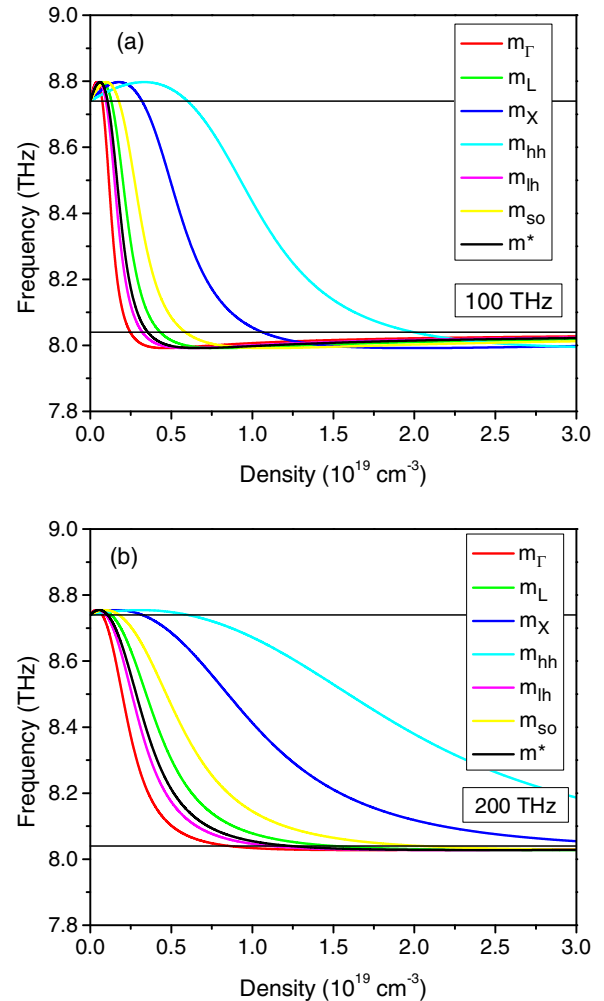


FIG. 11. (Color online) The calculated plasmon-phonon coupled mode frequency for the “phononlike”  $L_-$  mode at different photoexcitation densities for masses representing different carriers, which are created by 400 nm excitation of GaAs. Damping is (a) 100 THz; and (b) 200 THz.

phonon experiments on GaAs with 800 nm excitation, the properties of the  $L_-$  mode indicated substantially weaker damping by the fact that its frequency remained outside of the reststrahlen band. The dephasing of  $q = 0$  plasmons is determined by the momentum scattering of electrons and holes, which has been investigated in other ultrafast optical experiments. After the initial photoexcitation of carriers, several different types of scattering processes occur. These include intravalley ( $\Gamma \leftrightarrow \Gamma$ ,  $L \leftrightarrow L$ ) and intervalley scattering ( $\Gamma \leftrightarrow L$ ,  $\Gamma \leftrightarrow X$ ,  $L \leftrightarrow X$ ) within the conduction band, as well as inter- and intravalence band scattering [11,57]. For example, Becker *et al.* [58] and Brito *et al.* [59] report that for excitation in the  $\Gamma$  valley, interband polarization dephasing times decrease from 24 to 14 fs as the carrier density increases from  $1 \times 10^{18}$  to  $7 \times 10^{18} \text{ cm}^{-3}$ , which they attributed to the carrier momentum scattering and the carrier-carrier Coulomb interaction. Similarly, Kanasaki *et al.* [11] found fast ( $\sim 20$  fs) intervalley scattering from the  $\Gamma$  to  $L$  and  $X$  valleys through deformation potential interactions. In the case of 400 nm excitation, the plasma dominated by  $L$  valley electrons and

heavy holes is likely to experience momentum scattering on comparable or faster time scales, as will be evident from modeling of the coherent phonon dynamics [8,48,50,52].

### 1. Carrier ambipolar diffusion

In addition to scattering within and between bands and valleys, for 400 nm excitation the carrier diffusion plays an important role. Because the absorption length of 15 nm is quite small in relation to the sample thickness, the initial photoexcited carrier density has a strong gradient with respect to the distance  $z$  into the sample. The initially created exponentially decaying carrier density distribution into the sample is approximately given by

$$N(z, t = 0) = N_0 e^{-\alpha z}, \quad (5)$$

where  $\alpha$  is the absorption coefficient and  $N_0$  is the initial density of the chosen carrier type at the surface. Therefore, in order to describe the carrier dynamics, in addition to carrier scattering one must also account for their *diffusion* into the sample. For an infinite half-space with an initial exponential distribution, one can find an exact solution to the diffusion equation [60],

$$N(z, t) = \frac{N_0}{2} e^{\alpha^2 D t} \left[ e^{-\alpha z} \operatorname{erfc} \left( \frac{2\alpha D t - z}{\sqrt{4Dt}} \right) + e^{\alpha z} \operatorname{erfc} \left( \frac{2\alpha D t + z}{\sqrt{4Dt}} \right) \right], \quad (6)$$

where  $D$  is the carrier-specific diffusion constant and  $\operatorname{erfc}(x)$  is the complementary error function.

Because both electrons and holes are generated in equal numbers and they interact through the screened Coulomb field, they diffuse together in a process called ambipolar diffusion. The ambipolar diffusion constant for photoexcited carriers in undoped systems is given by

$$D_{\text{am}} = (\mu_h D_e + \mu_e D_h) / (\mu_e + \mu_h), \quad (7)$$

where  $D_e$  and  $D_h$  are the electron and hole diffusion constants and  $\mu_e$  and  $\mu_h$  are the corresponding carrier mobilities. Although ambipolar diffusion for band gap excitation into the  $\Gamma$  valley of GaAs has been studied [61,62], here we have to consider the case with a large transient population of carriers in the  $L$  and  $X$  valleys. In addition, the highest mobilities are typically known for undoped, semi-insulating material, and the mobility drops greatly with doping due to ionized impurity scattering. The diffusion constants and mobilities for the holes are somewhat better known. We estimate that the diffusion constants of electrons and holes at 300 K in GaAs are approximately given by  $D_e < 100 - 200 \text{ cm}^2 \text{ s}^{-1}$ ,  $D_h = 10 \text{ cm}^2 \text{ s}^{-1}$  [63].

Because the majority of the electrons are in the  $L$  valley, we can also estimate the diffusion constant of electrons from Ge where the lowest valley is the  $L$  valley; there the diffusion constant for electrons is  $D_e < 100 \text{ cm}^2 \text{ s}^{-1}$  [64], which is consistent with our previous estimate. Using these values for the electron and hole diffusion constants and assuming the electron mobility is 1 to 10 times greater than the hole mobility leads to an estimate of the ambipolar diffusion constant in the range from 15 to  $75 \text{ cm}^2 \text{ s}^{-1}$ . This is in agreement with Young

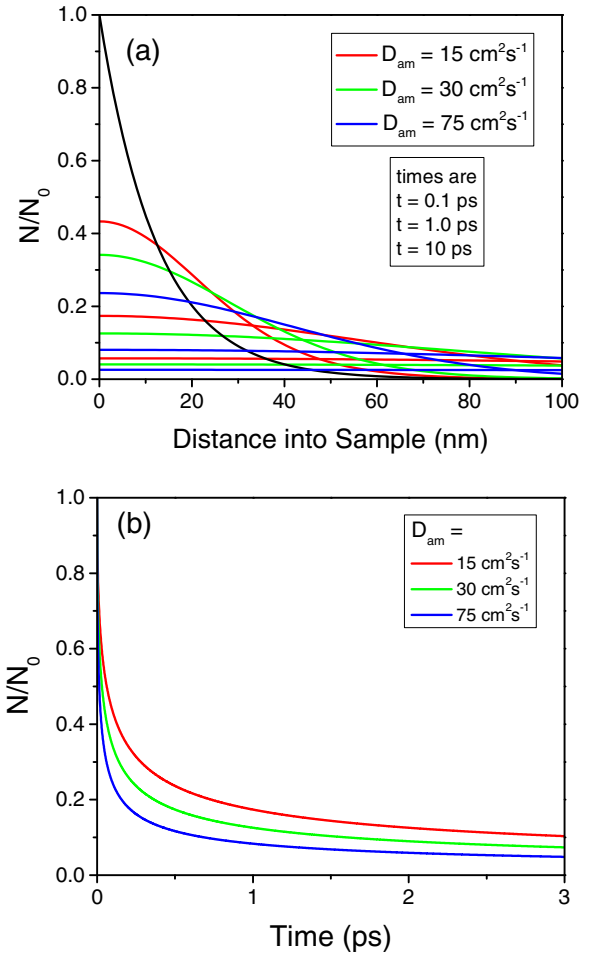


FIG. 12. (Color online) (a) Carrier density as a function of distance into the sample for three different ambipolar diffusion constants, 15, 30, and  $75 \text{ cm}^2 \text{ s}^{-1}$ . At  $t = 0$ , the density is an exponential distribution corresponding to the absorption depth of 15 nm (black line), independent of the diffusion constant. In time, the carrier density evolves to a more uniform distribution. The density profile is shown for three different times,  $t = 0.1, 1.0,$  and  $10.0$  ps. (b) Carrier density at the surface of the semiconductor as a function of time for diffusion constants, 15, 30, and  $75 \text{ cm}^2 \text{ s}^{-1}$ . As can be seen, the initial carrier density relaxes rapidly (nonexponentially) for the first few hundred femtoseconds. After 1 ps, less than 20% of the initial carriers remain at the surface for all three values of the diffusion constants.

and van Driel [65], who estimate the ambipolar diffusion constant in GaAs at room temperature to be  $20 \text{ cm}^2 \text{ s}^{-1}$  at low carrier densities, which increases to below  $80 \text{ cm}^2 \text{ s}^{-1}$  for carrier densities (in the  $\Gamma$  valley) greater than  $1 \times 10^{19} \text{ cm}^{-3}$ . Solutions to Eq. (6) are shown in Fig. 12(a) for different values of the ambipolar diffusion constant between 15– $75 \text{ cm}^2 \text{ s}^{-1}$ . The initial distribution at  $t = 0$  is an exponential decay with 15 nm corresponding to the absorption length of GaAs at 400 nm.

Transient reflectivity experiments are extremely sensitive to changes in the carrier density near the surface of the sample. The surface carrier density can be determined from Eq. (6) by setting the distance into the sample,  $z = 0$ . From Fig. 12(a), we see that the surface carrier density decreases to from 25 to 45% of its initial value in the first 100 fs depending on the value of

the diffusion constant. In Fig. 12(b), we plot the surface carrier density as a function of time for ambipolar diffusion constants 15, 30, and 75  $\text{cm}^2\text{s}^{-1}$ . As the carrier density changes, so do the frequencies of the coupled modes given in Eq. (1). Initially the carrier density at the surface decreases nonadiabatically, so there cannot be a well-defined coupled mode frequency in the first 100 fs, as is evident from the experimental time-dependent coupled mode frequency (Fig. 5). After the initial rapid decay, the carrier density changes on a time scale that is slower compared to the period of the normal modes. As a result, we can assume that the frequencies of the normal modes adiabatically follow the surface carrier density, given by

$$N(0, t) = N_o e^{\alpha^2 D_{\text{am}} t} \left[ \text{erfc} \left( \frac{2\alpha D_{\text{am}} t}{\sqrt{4D_{\text{am}} t}} \right) \right]. \quad (8)$$

We note that we have neglected surface recombination in Eq. (8). In principle, this could lead to an even faster decay of the surface carrier density.

### C. Calculations of time-dependent coupled mode frequencies

The dynamics of six types of carriers (three hole types, three electrons, etc.) with intra- and interband scattering and diffusion is beyond the scope of this paper. Instead, we focus just on the combined system of the  $L$  valley electrons and the heavy holes with  $m^*$  being the effective plasmon mass because most of the carriers are photoexcited in these phase space regions. We solve for the coupled-mode frequencies at the surface of the sample given by Eq. (3). We assume that the photoexcited electrons undergo ambipolar diffusion into the sample starting from the initial spatial distribution, which is given by Eq. (5), and use Eq. (8) to determine the surface plasma density as a function of time. We also assume that the coupled mode frequencies adiabatically follow the carrier density. We calculate the time-dependent frequencies of the two coupled modes as the carriers diffuse into the sample.

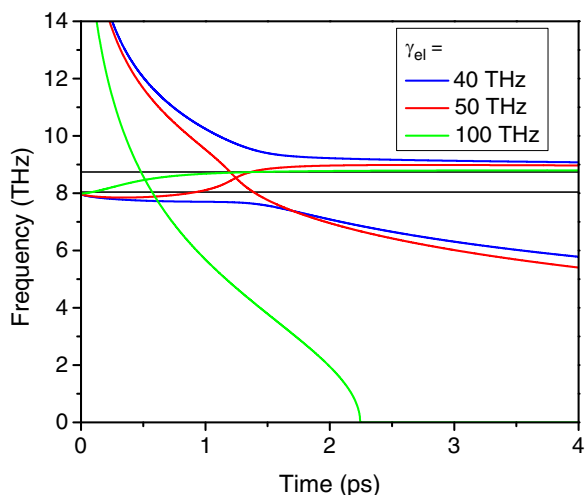


FIG. 13. (Color online) Coupled mode frequencies ( $L_+$  and  $L_-$ ) at the surface for combined  $L$  valley and heavy hole plasma with mass  $m^*$  with an initial carrier density of  $1.0 \times 10^{19} \text{cm}^{-3}$ . The plasma damping is varied from  $\gamma_{\text{el}} = 40, 50,$  and  $100 \text{THz}$ , and the diffusion constant is  $30 \text{cm}^2 \text{s}^{-1}$ .

In Fig. 13, we plot the frequencies of the  $L_+$  and  $L_-$  coupled modes as a function of time for an initial carrier density of  $1 \times 10^{19} \text{cm}^{-3}$  and a damping  $\gamma_{\text{el}} = 40, 50,$  and  $100 \text{THz}$ . As can be seen in all cases, initially the carrier density is high, and the LO-like mode is screened out to give the  $L_-$  mode at the TO frequency. As the carriers diffuse into the sample, the carrier density at the surface decreases. As already noted in Fig. 9, for  $\gamma_{\text{el}} = 40 \text{THz}$  there is no crossing of the roots, and no roots exist between the LO and TO frequencies. By contrast, for both the 50 and 100 THz cases, the stronger damping now confines the  $L_-$  mode predominantly between the LO and TO frequencies until the two modes cross. We note that for 100 THz, the plasmlike mode frequency goes to 0 at about 2.25 ps because at low density it is overdamped.

The plasma damping in the experimental system most likely falls in the range between  $\gamma_{\text{el}} = 100$  to  $200 \text{THz}$ . This corresponds to a momentum decay time of the plasmon (in the noninteracting limit) of 10 to 20 fs. The momentum decay time results from strong scattering of *both* the heavy holes as well as the  $L$  valley electrons, which have a large DOS.

In Fig. 14, we plot the  $L_+$  and  $L_-$  modes for initial densities varying between  $0.5 \times 10^{18} \text{cm}^{-3}$  and  $3.0 \times 10^{19} \text{cm}^{-3}$  for

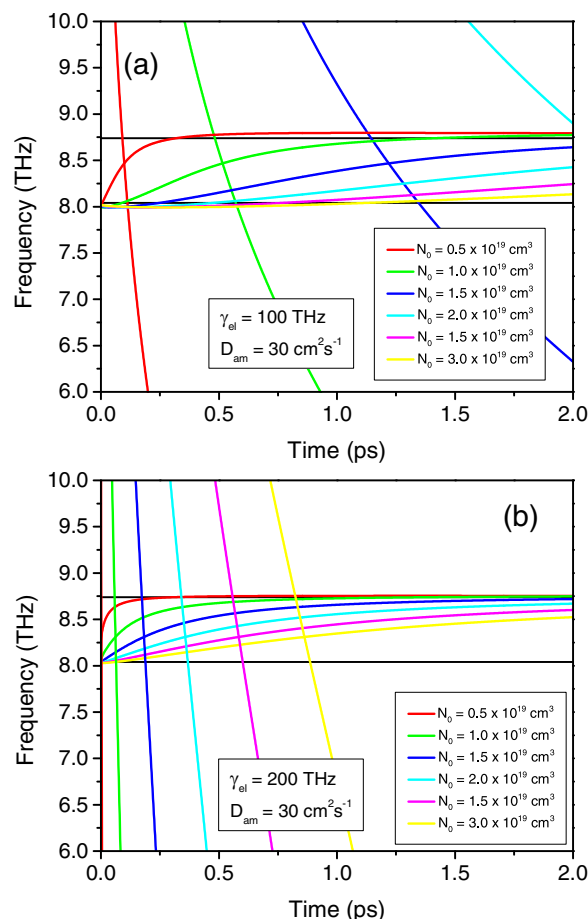


FIG. 14. (Color online) Coupled mode frequencies at the surface for the  $m^*$  plasmon mode ( $L$  valley and heavy hole) with ambipolar diffusion constant of  $30 \text{cm}^2\text{s}^{-1}$ . (a)  $\gamma_{\text{el}} = 100 \text{THz}$ , and  $N_0 = 0.5 - 3.0 \times 10^{19} \text{cm}^{-3}$ . (b)  $\gamma_{\text{el}} = 200 \text{THz}$ , and  $N_0 = 0.5 - 3.0 \times 10^{19} \text{cm}^{-3}$ .

(a)  $\gamma_{el} = 100$  THz and (b)  $\gamma_{el} = 200$  THz and an ambipolar diffusion constant of  $30 \text{ cm}^2\text{s}^{-1}$ . We see that for such high damping, at all densities the  $L_-$  solutions are between the LO and TO frequencies in accordance with experiments; the time scale for the transition from the TO to the LO frequency depends on the initial carrier concentration and is complete within the first 2 ps for all densities.

#### D. Differential reflectivity signal

Once we have established a model for the time-dependent coupled mode frequencies, as shown in Fig. 14, we can calculate their contribution to the differential reflectivity signal. Assuming that the frequency of the mode is slowly varying, which is valid after the first 100 fs, we can then use the adiabatic approximation to estimate the contribution from a given mode:

$$\frac{\Delta R}{R} \sim C \exp\left(-i \int_0^t \text{Re}[\omega(N(0,t))] dt - \int_0^t \text{Im}[\omega(N(0,t))] dt\right). \quad (9)$$

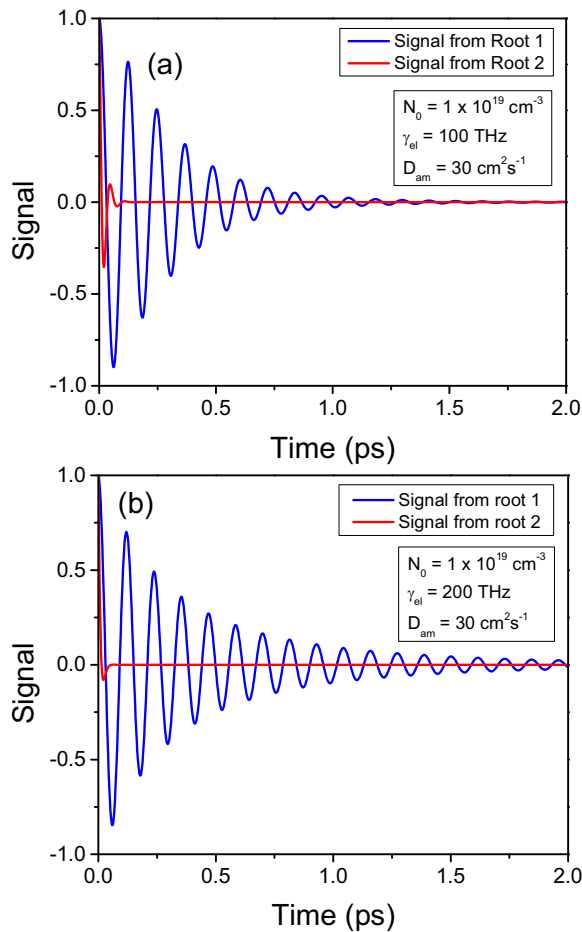


FIG. 15. (Color online) Contributions to the differential reflectivity signal (Eq. 9) from the plasmonlike (red) and phononlike (blue) modes. (a) Weaker damping ( $\gamma_{el} = 100$  THz) and initial surface carrier density of  $1 \times 10^{19} \text{ cm}^{-3}$ . (b) Stronger damping ( $\gamma_{el} = 200$  THz) and initial surface carrier density of  $1 \times 10^{19} \text{ cm}^{-3}$ . The diffusion constant in both cases is  $D_{am} = 30 \text{ cm}^2\text{s}^{-1}$ .

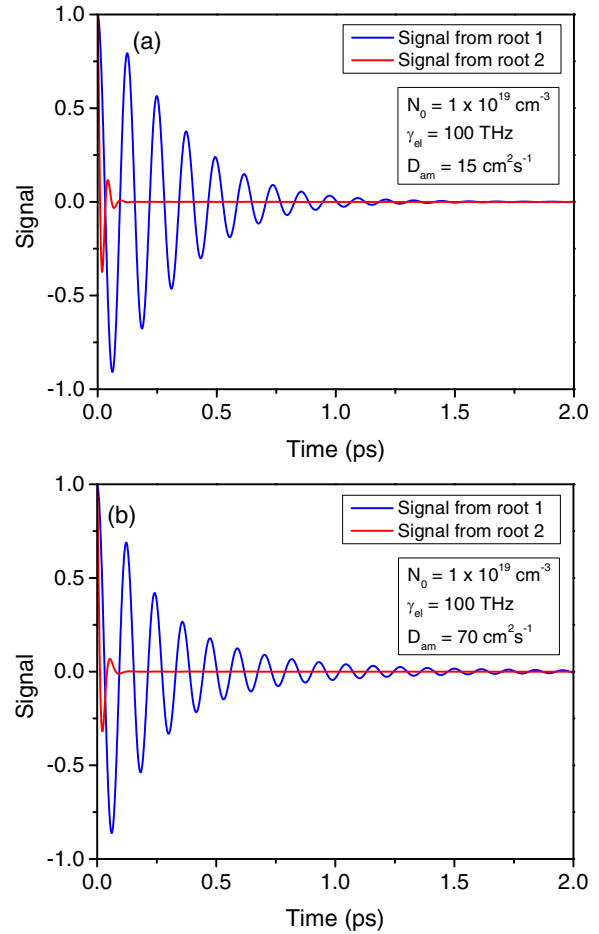


FIG. 16. (Color online) Effect of diffusion on the signal for the plasmonlike (red) and phononlike (blue) modes for  $\gamma_{el} = 100$  THz, initial carrier density  $1 \times 10^{19} \text{ cm}^{-3}$ . (a)  $D_{am} = 15 \text{ cm}^2\text{s}^{-1}$ . (b)  $D_{am} = 70 \text{ cm}^2\text{s}^{-1}$ .

Here  $C$  is a coupling constant that determines how strongly the mode couples to the reflectivity. In previous work, Kuznetsov and Stanton found the coupling ratio to be  $-2.7$  for the plasmonlike mode with respect to the phononlike mode [26]. We note that the exponential contains *integrals* over the real and imaginary parts of the mode frequencies. This is similar to the Wentzel–Kramers–Brillouin (WKB) approximation from quantum mechanics, where the integral is needed to keep track of the overall phase and damping of the oscillation [66].

In Fig. 15, we show the signals (normalized initially to 1) from the plasmonlike and phononlike modes. Figure 15(a) corresponds to a damping  $\gamma_{el} = 100$  THz, while Fig. 15(b) corresponds to stronger damping  $\gamma_{el} = 200$  THz. The initial surface carrier density is  $1.0 \times 10^{19} \text{ cm}^{-3}$ . We see that the plasmonlike  $L_+$  mode (red) is damped out quicker for the 200 THz case, as expected. The phononlike  $L_-$  mode (blue), however, appears to damp out quicker for the 100 THz case. At first this might seem counterintuitive, but we can understand this effect from Fig. 9(b). The decay of the phononlike mode is not determined solely by  $\gamma_{ph}$  but also includes the mixing of the two modes. In Fig. 9(b), we see that the larger damping (in the first 2 ps) for the phononlike mode occurs for the *smaller*

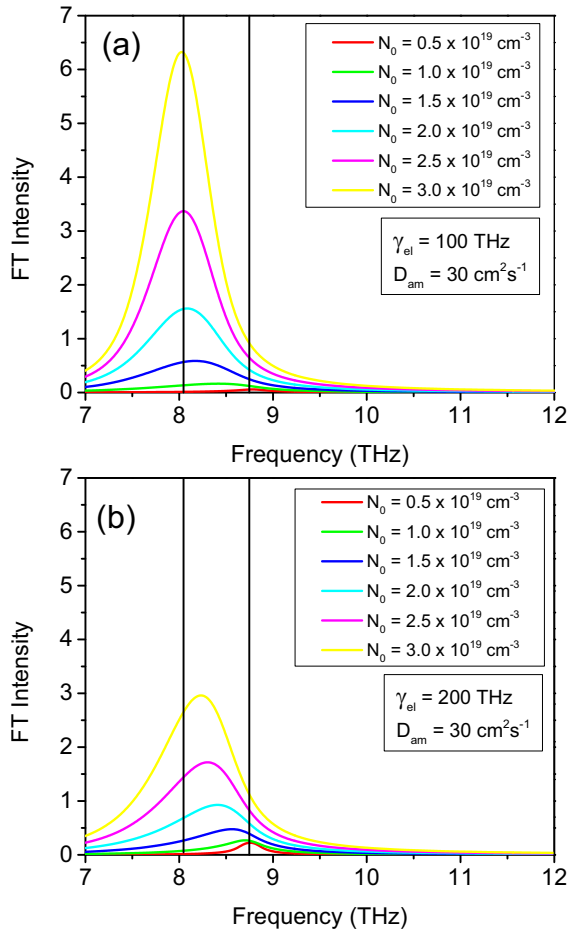


FIG. 17. (Color online) FT power spectra for different carrier damping and initial surface excitation. (a) The weaker damping ( $\gamma_{el} = 100 \text{ THz}$ ) and initial surface carrier densities range from  $0.5 - 3.0 \times 10^{19} \text{ cm}^{-3}$ . (b) The stronger damping ( $\gamma_{el} = 200 \text{ THz}$ ) and initial carrier densities range from  $0.5 - 3.0 \times 10^{19} \text{ cm}^{-3}$ . The diffusion constant is  $D_{am} = 30 \text{ cm}^2 \text{ s}^{-1}$  in both cases. The vertical lines denote the TO and LO phonon frequencies.

value of  $\gamma_{el}$ . Simply stated, the  $L_-$  mode is more phononlike, including its damping for the higher plasmon damping.

In Fig. 16, we show the signal for the  $L_+$  plasmonlike (red) and  $L_-$  phononlike (blue) modes for  $\gamma_{el} = 100 \text{ THz}$  and two different values for the diffusion constant: 15 and  $70 \text{ cm}^2 \text{ s}^{-1}$  to examine the effects of diffusion. As we saw in Fig. 14, the larger diffusion constant causes the two modes to cross at an earlier time, which leads to less damping of the  $L_-$  mode for the higher value of the diffusion constant in Fig. 16 [41].

Once we have obtained the time domain signal, we can take the FT and plot the absolute square of the FT. We plot the Fourier intensities in Fig. 17 for several values of the initial surface density ranging from  $5 \times 10^{18}$  to  $3 \times 10^{19} \text{ cm}^{-3}$  and a diffusion constant of  $30 \text{ cm}^2 \text{ s}^{-1}$ . In (a), the damping is  $\gamma_{el} = 100 \text{ THz}$ , and in (b) it is  $\gamma_{el} = 200 \text{ THz}$ . We have plotted the Fourier intensity for the phononlike modes (blue curves in Fig. 15). We see that in both cases, at higher initial densities, the FT spectra are peaked between the LO and TO frequencies, as observed in the experiments.

In Fig. 18, we show the time domain reflectivity signal (a) and the calculated Fourier intensity (b) for densities ranging from  $0.6 \times 10^{18}$  to  $2.1 \times 10^{19} \text{ cm}^{-3}$  and with  $\gamma_{el} = 150 \text{ THz}$  and  $D_{am} = 15 \text{ cm}^2 \text{ s}^{-1}$ . These values seem to produce the best qualitative agreement with the experimental curves, shown in Fig. 2 and Fig. 3. We include the effects of both modes (the phononlike and plasmonlike modes), with the plasmon mode having an initial amplitude of  $-2.7$  times the phononlike mode [26]. As can be seen, the inclusion of the plasmonlike mode gives the initial derivative like feature near  $t = 0$ .

While the agreement between the theoretical calculations and experiment looks qualitatively and even semiquantitatively correct, it is important to note that the theoretical calculations are done at a *single peak* carrier density. In the experiment, the laser pulse has a Gaussian profile in the lateral direction on the surface. As a result, the theoretical calculations should be averaged over a Gaussian distribution of densities. Only the center of the Gaussian would have the highest densities, and the wings would have a much smaller density. In fact, we believe that some of the signal at longer times  $> 2 \text{ ps}$  at the LO frequency comes from the low density wings of the pulse spatial profile on the surface plane [51]. At these densities, the coupling between the plasma and phonons is very weak, and hence the decay rate of the LO mode approaches the bare LO phonon damping term  $\gamma_{ph}$ . In contrast, at higher carrier densities, the damping of the phononlike mode will be higher due to the stronger coupling with the highly damped plasma mode.

## V. DISCUSSION AND CONCLUSIONS

Here we discuss the main characteristics of the transient anisotropic reflectivity and the corresponding FT spectra at various carrier density levels. The main characteristic of 400 nm excitation at the  $E_1$  gap is the creation of a high-density  $L$  valley electron-heavy hole plasma within the shallow absorption depth (15 nm) from the GaAs surface. These features define the photogenerated plasma screening, frequency, dephasing, and diffusion characteristics. The main feature of the time domain signal is a highly damped oscillation between 0.2–2 ps time delay followed by a weaker but long-lived oscillation at the bare LO phonon frequency. The FT spectra contain two main features, which we attributed to the  $L_-$  and LO phonon modes. The LO mode frequency does not change, but the time-integrated  $L_-$  frequency changes from near the LO frequency to near the TO frequency with increasing initial photoexcited carrier density. This is somewhat unusual since in several previous experiments on  $n$ -doped GaAs, the coupling of LO phonon with the  $\Gamma$  valley electrons caused the  $L_-$  frequency to shift from *below* TO toward the TO limit (8.0 THz) as the carrier density was increased [31,40,50]. The appearance of the  $L_-$  mode between the TO and LO modes might be considered as anomalous, but in fact it is characteristic of the *strong* damping of heavy carrier plasmas. Indeed, in Raman scattering experiments on  $p$ -doped GaAs [30,42–44], this same trend where the  $L_-$  mode shifts from the LO to the TO limits was observed and was attributed to the strong hole-plasmon damping. In our case, the frequency change of the  $L_-$  mode is analyzed by considering highly damped plasmon-phonon coupling with contributions to the damping from both the heavy hole plasma and the conduction

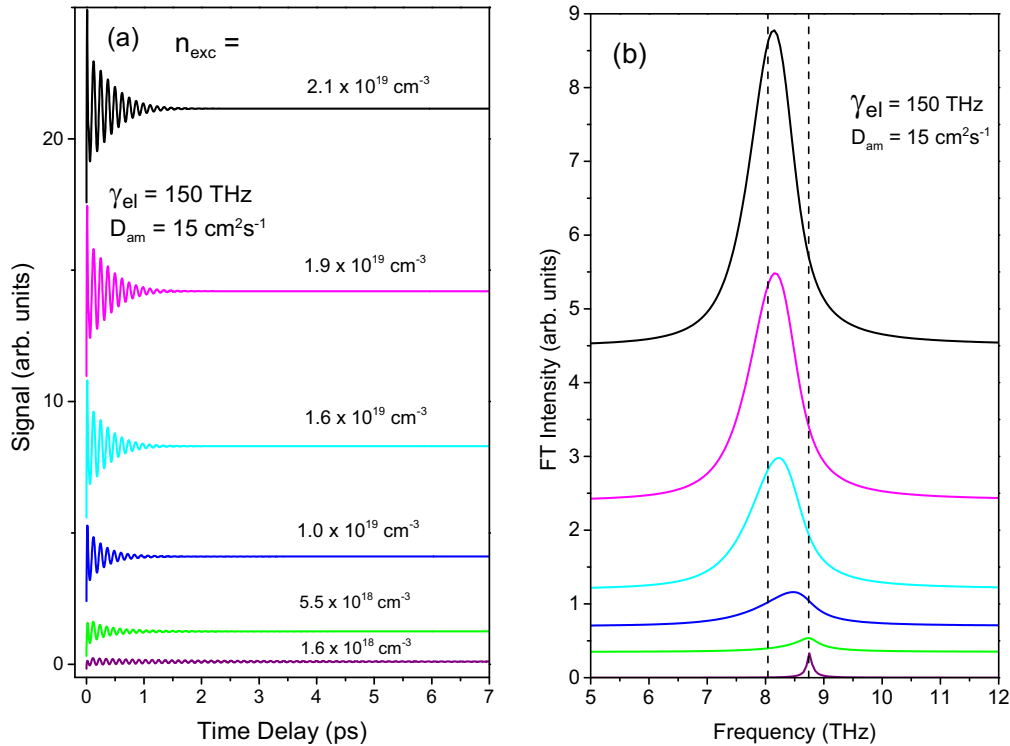


FIG. 18. (Color online) (a) The calculated reflectivity signals and (b) FT intensities including both the phononlike and plasmonlike modes with the plasmlike mode being weighted by a factor of  $-2.7$ . As can be seen, inclusion of the plasmlike mode gives the initial derivative-like signal close to zero time. The signal is calculated for densities ranging from  $1.6 \times 10^{18}$  to  $2.1 \times 10^{19} \text{ cm}^{-3}$ . The damping is  $150 \text{ THz}$ , and the diffusion constant is  $15 \text{ cm}^2\text{s}^{-1}$ .

band satellite  $L$  valley electron plasma. We conclude that the strong damping of the combined  $L$  valley electron and heavy hole plasmon leads to the  $L_-$  frequency behavior. Such high damping in this case contrasts with the experiments for the  $E_0$  gap excitation with infrared-visible light, where the relatively slower damping of the lighter carriers in the  $\Gamma$  valley of  $n$ -doped GaAs lead to the textbook plasmon-phonon coupling behavior.

By analyzing the experimental data and comparing it with a theoretical model that describes the time-dependent coupling of the coherent phonon and the electron-hole plasma as the photoexcited carriers diffuse into the sample on a picosecond time scale, we find that diffusion is important because with the  $15 \text{ nm}$  absorption depth of the pump pulse, it is the dominant process that changes the plasma density on the time scale of the coherent phonon oscillations. As the photoexcited carriers rapidly diffuse into the sample away from the surface, the density-dependent plasmon-phonon coupling changes, which leads to a time-dependent frequency of the observed oscillations. The calculated phonon-plasmon dynamics qualitatively reproduces the experimentally observed time-dependent frequency. Mics *et al.* [67] also report evidence for strongly diffusion-dependent electron dynamics on a picosecond time scale in a recent  $400 \text{ nm}$  pump-THz probe experiment.

The FT intensities are analyzed as a function of the carrier density. The  $L_-$  intensity increases with the carrier density because the plasmon component dominates the coupled mode behavior. It is observed that LO phonon peak intensity first increases with carrier density. But it saturates with further

increase of the carrier density, showing that the screening of the depletion electric field is complete. As a result, the strength of the coherent phonon generation is also saturated, and the peak intensity does not increase with increasing carrier density. A sublinear increase of intensity of the reflectivity signal was also observed in the case of GaAs with  $800 \text{ nm}$  excitation [13]. Both the  $L_-$  and LO mode intensities were sublinear in similar studies, with  $800 \text{ nm}$  excitation, though at lower carrier densities [31,50,68]. Here, we distinctly observe two regimes of carrier density showing increasing screening effects with increasing carrier density.

The coupled modes described in the present theoretical model are adiabatically coupled, whereas they actually form on the time scale of the inverse plasma frequency [2,50]. The screening dynamics not described in the model may be responsible for the effective coherent oscillation frequency below  $\omega_{TO}$  that is observed in the windowed FT spectra in Fig. 5. This observation may be related to the delayed formation of the coupled modes due to the relatively slow screening in photodoped semiconductors [50].

To conclude, we have observed the sublinear carrier density-dependence behavior of the coherent phonon intensity in bulk GaAs photoexcited with a  $400 \text{ nm}$  pump pulse. This indicates that the dispersive force associated with screening of the depletion field is the dominant force behind the coherent phonon generation. We found the following: (i) the  $L_-$  mode frequency lies *between* the TO and LO frequencies, indicating that the plasmon (composed of both satellite  $L$  valley electrons and heavy holes) is strongly damped; (ii)

the absorption length is short (15 nm), and, as a result, diffusion of carriers away from the surface rapidly changes the carrier density (and hence the plasmon-phonon coupling) as a function of time; and (iii) the evolution of the decay time and frequency with increasing density indicate that the dynamics are dominated by the carrier momentum scattering time involving the heavy holes and the satellite  $L$  valley electrons.

## ACKNOWLEDGMENTS

This paper was supported by the National Science Foundation (NSF) through Grants No. CHE-0650756, No. DMR-1311845 (Petek), and No. DMR-1311849 (Stanton). We thank Ben Hu for the useful discussion about coupled electron-hole plasmons.

- 
- [1] A. Leitenstorfer, C. Fürst, A. Laubereau, W. Kaiser, G. Tränkle, and G. Weimann, *Phys. Rev. Lett.* **76**, 1545 (1996).
- [2] R. Huber, F. Tauser, A. Brodschelm, M. Bichler, G. Abstreiter, and A. Leitenstorfer, *Nature* **414**, 286 (2001).
- [3] M. Hase, M. Kitajima, A. M. Constantinescu, and H. Petek, *Nature* **426**, 51 (2003).
- [4] V. M. Axt and T. Kuhn, *Rep. Prog. Phys.* **67**, 433 (2004).
- [5] X. Cui, C. Wang, A. Argondizzo, S. Garrett-Roe, B. Gumhalter, and H. Petek, *Nat. Phys.* **10**, 505 (2014).
- [6] L. Rota, P. Lugli, T. Elsaesser, and J. Shah, *Phys. Rev. B* **47**, 4226 (1993).
- [7] A. Leitenstorfer, S. Hunsche, J. Shah, M. C. Nuss, and W. H. Knox, *Phys. Rev. Lett.* **82**, 5140 (1999).
- [8] M. Hase, S.-I. Nakashima, K. Mizoguchi, H. Harima, and K. Sakai, *Phys. Rev. B* **60**, 16526 (1999).
- [9] P. Gaal, W. Kuehn, K. Reimann, M. Woerner, T. Elsaesser, and R. Hey, *Nature* **450**, 1210 (2007).
- [10] K. W. Stone, D. B. Turner, K. Gundogdu, S. T. Cundiff, and K. A. Nelson, *Acc. Chem. Res.* **42**, 1452 (2009).
- [11] J. I. Kanasaki, H. Tanimura, and K. Tanimura, *Phys. Rev. Lett.* **113**, 237401 (2014).
- [12] T. Pfeifer, W. Kütt, H. Kurz, and R. Scholz, *Phys. Rev. Lett.* **69**, 3248 (1992).
- [13] T. Pfeifer, T. Dekorsy, W. Kütt, and H. Kurz, *Appl. Phys. A* **55**, 482 (1992).
- [14] G. A. Garrett, T. F. Albrecht, J. F. Whitaker, and R. Merlin, *Phys. Rev. Lett.* **77**, 3661 (1996).
- [15] M. Hase, O. V. Misochko, and K. Ishioka, in *Dynamics at Solid State Surfaces and Interfaces, Vol. 1: Current Developments*, edited by U. Bovensiepen, H. Petek, and M. Wolf (Wiley-VCH Verlag GmbH & Co., Weinheim, 2010), p. 213.
- [16] M. Hase, M. Katsuragawa, A. M. Constantinescu, and H. Petek, *Nat. Photon* **6**, 243 (2012).
- [17] S. Wall, D. Wegkamp, L. Foglia, K. Appavoo, J. Nag, R. F. Haglund, J. Stähler, and M. Wolf, *Nat Commun.* **3**, 721 (2012).
- [18] M. Hase, M. Katsuragawa, A. M. Constantinescu, and H. Petek, *New J. Phys.* **15**, 055018 (2013).
- [19] R. Kersting, J. N. Heyman, G. Strasser, and K. Unterrainer, *Phys. Rev. B* **58**, 4553 (1998).
- [20] A. Pashkin, C. Kübler, H. Ehrke, R. Lopez, A. Halabica, R. F. Haglund, R. Huber, and A. Leitenstorfer, *Phys. Rev. B* **83**, 195120 (2011).
- [21] D. Wegkamp, M. Herzog, L. Xian, M. Gatti, P. Cudazzo, C. L. McGahan, R. E. Marvel, R. F. Haglund, Jr., A. Rubio, M. Wolf, and J. Stähler, *Phys. Rev. Lett.* **113**, 216401 (2014).
- [22] T. E. Stevens, J. Kuhl, and R. Merlin, *Phys. Rev. B* **65**, 144304 (2002).
- [23] W. A. Kütt, W. Albrecht, and H. Kurz, *IEEE J. Quantum Electron.* **28**, 2434 (1992).
- [24] H. J. Zeiger, J. Vidal, T. K. Cheng, E. P. Ippen, G. Dresselhaus, and M. S. Dresselhaus, *Phys. Rev. B* **45**, 768 (1992).
- [25] A. V. Kuznetsov and C. J. Stanton, *Phys. Rev. Lett.* **73**, 3243 (1994).
- [26] A. V. Kuznetsov and C. J. Stanton, *Phys. Rev. B* **51**, 7555 (1995).
- [27] G. C. Cho, W. Kütt, and H. Kurz, *Phys. Rev. Lett.* **65**, 764 (1990).
- [28] T. Dekorsy, T. Pfeifer, W. Kütt, and H. Kurz, *Phys. Rev. B* **47**, 3842 (1993).
- [29] M. Hase, K. Mizoguchi, H. Harima, F. Miyamaru, S. Nakashima, R. Fukasawa, M. Tani, and K. Sakai, *J. Lumin.* **76–77**, 68 (1998).
- [30] Y. M. Chang, *Appl. Phys. Lett.* **80**, 2487 (2002).
- [31] K. Ishioka, A. K. Basak, and H. Petek, *Phys. Rev. B* **84**, 235202 (2011).
- [32] F. Cerdeira and M. Cardona, *Phys. Rev. B* **5**, 1440 (1972).
- [33] T. Sjödin, H. Petek, and H.-L. Dai, *Phys. Rev. Lett.* **81**, 5664 (1998).
- [34] P. Lautenschlager, M. Garriga, S. Logothetidis, and M. Cardona, *Phys. Rev. B* **35**, 9174 (1987).
- [35] O. J. Glembocki and F. H. Pollak, *Phys. Rev. Lett.* **48**, 413 (1982).
- [36] D. W. Bailey, C. J. Stanton, and K. Hess, *Phys. Rev. B* **42**, 3423 (1990).
- [37] S. M. Sze and K. K. Ng, *Physics of Semiconductor Devices* (Wiley-Interscience, Hoboken, NJ, 2007).
- [38] D. E. Aspnes and A. A. Studna, *Phys. Rev. B* **27**, 985 (1983).
- [39] The experimental carrier density  $n_{\text{exc}}$  is inhomogeneous over the approximately Gaussian intensity distribution of the laser pulse and due to the steep absorption gradient normal to the sample surface. The reported experimental carrier densities  $n_{\text{exc}}$  are the peak carrier densities. The theoretical carrier densities  $n$  are spatially invariant or represent the surface density of an exponentially decaying photoexcited profile, depending on the simulated property.
- [40] M. Hase, K. Ishioka, M. Kitajima, and K. Ushida, *Appl. Phys. Lett.* **82**, 3668 (2003).
- [41] The  $L_+$  mode is plasmonlike at high carrier densities when the bare plasma frequency is above the LO phonon frequency. Through diffusion, the plasma frequency falls below the LO phonon frequency, and the  $L_+$  mode becomes phononlike.
- [42] K. Wan and J. F. Young, *Phys. Rev. B* **41**, 10772 (1990).
- [43] R. Fukasawa and S. Perkowitz, *Phys. Rev. B* **50**, 14119 (1994).
- [44] G. Irmer, M. Wenzel, and J. Monecke, *Phys. Rev. B* **56**, 9524 (1997).
- [45] A. K. Basak, Ph.D. dissertation, University of Pittsburgh, 2010.
- [46] A. M. Constantinescu, Ph.D. dissertation, University of Pittsburgh, 2010.

- [47] P. Babilotte, P. Ruello, G. Vaudel, T. Pezeril, D. Mounier, J.-M. Breteau, and V. Gusev, *Appl. Phys. Lett.* **97**, 174103 (2010).
- [48] F. Vallée, F. Ganikhanov, and F. Bogani, *Phys. Rev. B* **56**, 13141 (1997).
- [49] N. Nintunze and M. A. Osman, *Phys. Rev. B* **50**, 10706 (1994).
- [50] J. Hu, O. V. Misochko, A. Goto, and K. G. Nakamura, *Phys. Rev. B* **86**, 235145 (2012).
- [51] G. C. Cho, T. Dekorsy, H. J. Bakker, R. Hövel, and H. Kurz, *Phys. Rev. Lett.* **77**, 4062 (1996).
- [52] M. A. Osman and D. K. Ferry, *Phys. Rev. B* **36**, 6018 (1987).
- [53] G. Irmer, M. Wenzel, and J. Monecke, *Phys. Stat. Sol. (b)* **195**, 85 (1996).
- [54] D. W. Bailey and C. J. Stanton, *J. Appl. Phys.* **77**, 2107 (1995).
- [55] M. Woerner and T. Elsaesser, *Phys. Rev. B* **51**, 17490 (1995).
- [56] P. Y. Yu and M. Cardona, *Fundamentals of Semiconductors* (Springer-Verlag, Berlin, 2003).
- [57] B. H. Bairamov, I. P. Ipatova, and V. A. Voitenko, *Phys. Rep.* **229**, 221 (1993).
- [58] P. C. Becker, H. L. Fragnito, C. H. B. Cruz, R. L. Fork, J. E. Cunningham, J. E. Henry, and C. V. Shank, *Phys. Rev. Lett.* **61**, 1647 (1988).
- [59] C. H. Brito Cruz, J. P. Gordon, P. C. Becker, R. L. Fork, and C. V. Shank, *IEEE J. Quantum Electron.* **24**, 261 (1988).
- [60] C. J. Cook, S. Khan, G. D. Sanders, X. Wang, D. H. Reitze, Y. D. Jho, Y. W. Heo, J. M. Erie, D. P. Norton, and C. J. Stanton, *Proc. SPIE* **7603**, 760304 (2010).
- [61] B. A. Ruzicka, L. K. Werake, H. Samassekou, and H. Zhao, *Appl. Phys. Lett.* **97**, 262119 (2010).
- [62] K. Chen, W. Wang, J. Chen, J. Wen, and T. Lai, *Opt. Express* **20**, 3580 (2012).
- [63] J. S. Blakemore, *J. Appl. Phys.* **53**, R123 (1982).
- [64] C. Jacoboni, F. Nava, C. Canali, and G. Ottaviani, *Phys. Rev. B* **24**, 1014 (1981).
- [65] J. F. Young and H. M. van Driel, *Phys. Rev. B* **26**, 2147 (1982).
- [66] D. J. Griffiths, *Introduction to Quantum Mechanics* (Pearson Education Inc./Prentice Hall, Upper Saddle River, New Jersey, 2005).
- [67] Z. Mics, A. D'Angio, S. A. Jensen, M. Bonn, and D. Turchinovich, *Appl. Phys. Lett.* **102**, 231120 (2013).
- [68] K. Ishioka, M. Kitajima, and K. Ushida, *J. Phys. Soc. Jap.* **75**, 084704 (2006).